Nanostructure Evolution in a Poly(ether ester) Elastomer during Drawing and the Displacement of Hard Domains from Lamellae

NORBERT STRIBECK,[1] SÉRGIO S. FUNARI[2]

[1] Institute of Technical and Macromolecular Chemistry, University of Hamburg, Bundesstrasse 45, 20146 Hamburg, Germany

[2] Max-Planck Institute of Colloids and Interfaces, c/o HASYLAB, 22603 Hamburg, Germany

Received 20 March 2003; revised 23 April 2003; accepted 24 April 2003

ABSTRACT: A poly(ether ester) thermoplastic elastomer with a soft block content of 50 wt % has been studied with synchrotron small-angle X-ray scattering (SAXS) during strain/relaxation cycles. The rigid nodes of the elastic network are not the hard domains themselves but instead are ordered three-dimensional assemblies of several hard domains. At a critical elongation, single hard domains are disrupted and dislocated from these assemblies in a peculiar manner. In the ultimate structure, remaining pairs of hard domains form (semi)elastic nodes. The complex two-dimensional SAXS patterns indicate stacks from tilted lamellae that are destroyed when the sample is strained to double its initial length. With multidimensional chord distribution function analysis, the complex nanostructure and its evolution in the draw experiment have been analyzed. The fundamental hard domains are not lamellae but cylinders (5 nm $\times$ 8 nm) arranged on a lattice at cylindrical coordinates (r_{12}, r_3), which are given by the intersections of $r_3(r_{12}) = \pm 1.5 r_{12} \pm 13\text{nm}n$, n being a natural number. A semielastic component is made from hard domains forming other lamellar assemblies, which are characterized by $n = 3/2$. © 2003 Wiley Periodicals, Inc. J Polym Sci Part B: Polym Phys 41: 1947–1954, 2003

Keywords: thermoplastics; elastomers; drawing; SAXS; morphology

INTRODUCTION

Thermoplastic elastomers are generally prepared from two types of long-chain segments. Soft blocks are distinguished by low melting and glass-transition temperatures, whereas hard blocks exhibit high glass-transition temperatures or are crystallizable. Phase separation takes place when the polymer is cooled from the melt, and hard domains formed in a soft matrix act as nodes in a more or less elastic network.[1] Both the extension of the domains and the distances among them are on the order of several nanometers. Therefore, these materials must be considered filled elastic networks, and their mechanical properties depend not only on the polymer chain structure but also on the shape and arrangement of the hard domains in the matrix and their response to a load. In principle, the nanoscopic processes were labeled many decades ago (e.g., void formation[2,3] and microfibrillation[4]). If we understand how these processes work and how they are intertwined, we will be able both to better assess the capacity of the material and to tailor the material properties by proper processing.

Correspondence to: N. Stribeck (E-mail: norbert.stribeck@desy.de)

Journal of Polymer Science: Part B: Polymer Physics, Vol. 41, 1947–1954 (2003)

Thermoplastic elastomers are attractive for structural investigations not only because of their peculiar mechanical properties but also because they offer many modeling opportunities on account of their crystallizability, multiblock character, and possibility of varying both the block flexibility and length. There are also many unanswered questions concerning the deformation mechanism of this class of polymers in comparison with classical rubbers. For this reason, the relationship between macrodeformation and microdeformation was systematically studied during the last decade[5–10] by means of small-angle X-ray scattering (SAXS). All studies were carried out on polyblock poly(ether ester)s (PEEs).

Many methods can be used to investigate nanostructure, but few are as suitable as X-ray methods to be integrated into processing. However, there are several problems to be solved. First, the structure evolution has to be monitored with sufficient time resolution. Therefore, strong X-ray sources such as synchrotrons are required. Second, scattering studies are linked to a fundamental handicap. Information concerning the nanostructure is not suggestive as that from microscopy. For conclusions to be drawn concerning physical space, an inversion is necessary, either by analysis or by interpretation. Because no multidimensional SAXS method was available, in previous studies we focused on partial aspects[11] of the nanostructure and developed methods for their quantitative analysis, such as for the longitudinal structure[12] or transverse structure.[13] Here we demonstrate how the method of multidimensional chord distribution function (CDF) analysis[14] can be used to enlighten the process of straining a PEE on a nanoscopic scale.

Comparative *in situ* drawing studies of such bulk materials by both reciprocal and direct space techniques during drawing would be desirable, but they are extremely difficult to carry out, as demonstrated in the only article found in the literature that approaches this problem.[15]

EXPERIMENTAL

Material

Arnitel E 1500/50 (manufactured by DSM, the Netherlands) is a PEE consisting of poly(butylene terephthalate) as hard segments and poly(tetrahydrofuran) (PTHF) as soft segments (PTHF weight-average molecular weight = 1500 g/mol, ϕ_{PTHF} = 50 wt %).

From the commercial material, a film 0.52 mm thick was prepared in a hydraulic press. Pellets were melted at a temperature of 270 °C for 3 min. Thereafter, the melt was pressed for 1 min at 50 bar. Rectangular strips (50 mm × 12 mm) were cut from the films for the SAXS measurements.

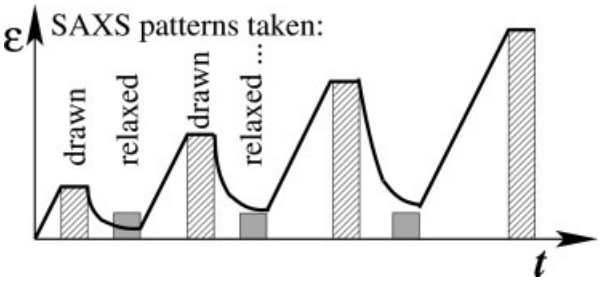

Figure 1. Sketch of the straining experiment [$\epsilon(t)$]. The time intervals during which SAXS patterns were recorded are indicated by bars.

SAXS and Drawing

Synchrotron radiation with a wavelength of λ = 0.15 nm, generated at the A2 beam line of HASYLAB (Hamburg, Germany), was applied. The sample-to-detector distance was set to 1525 mm. Two-dimensional (2D) SAXS patterns [$I(s_{12}, s_3)$] were registered on image plates exposed for 2 min. An area of 1000 pixels × 1000 pixels, each with a size of 176 mm × 176 mm, was read out and used for data evaluation. The maximum radius of the circular sensitive area of the detector was s_{max} = 0.38 nm^{-1}, with the modulus of the scattering vector defined by $s = (s_{12}^2 + s_3^2)^{0.5} = (2/\lambda)\sin\theta$ and the scattering angle being 2θ.

A straining stage (courtesy of B. Heise, University of Ulm) mounted in the pathway of the X-ray beam allowed for controlled elongation cycling of the sample (Fig. 1). After the elongation was increased to the next step, a scattering pattern (drawn) was recorded under constant strain. Then, the sample was released, the image plate was exchanged, and a pattern in the relaxed state was taken, followed by a measurement under stress at a higher elongation ($\Delta\epsilon \approx 0.2$). The elongation is defined as $\epsilon = (\ell - \ell_0)/\ell_0$, with ℓ and ℓ_0 being the actual and initial distances between two marks on the sample, respectively.

SAXS Data Evaluation

Images were normalized with respect to the incident flux, and blind areas were masked. The in-

strument background was subtracted, with consideration given to sample absorption. The center and orientation of the patterns were determined. As the final step of preprocessing, the patterns were aligned and averaged with respect to the four quadrants.

Postprocessing was performed similarly to a procedure described in earlier works.[14,16] Strained samples were processed to yield the three-dimensional chord distribution [$z(r_{12}, r_3)$] with cylindrical symmetry. The positions of the maxima and minima in $z(r_{12}, r_3)$ were determined. On the basis of these data, conclusions on the nanostructure were drawn.

In detail, remnant blind spots were filled in the preprocessed scattering intensity [$I(s_{12}, s_3)$] with 2D extrapolation by radial basis functions.[17] With the same procedure, data were extrapolated to fill the cylindrical volume [$-0.55\ \mathrm{nm}^{-1} < s_{12}, s_3 < 0.55\ \mathrm{nm}^{-1}$].

As pointed out in several articles,[14,18,19] the CDF is computed from the scattering intensity [$I(\mathbf{s})$] by

$$z(r_1, r_3) = \mathcal{F}^2[L(\mathbf{s})\{I(\mathbf{s})\}_2(s_1, s_3) - B(s_1, s_3)] \qquad (1)$$

with the projection of the scattering intensity on the representative (s_1, s_3) plane:

$$\{I(\mathbf{s})\}_2(s_1, s_3) = \int I(\mathbf{s}) ds_2 \qquad (2)$$

The factor $L(\mathbf{s}) = -4\pi^2(s_1^2 + s_3^2)$ is equivalent to the Laplacian in physical space, $B(s_1, s_{,3})$, describes a background determined by iterated spatial frequency filtering of $-L(\mathbf{s})\{I(\mathbf{s})\}_2(s_1, s_3)$, and $\mathcal{F}^2()$ denotes a 2D Fourier transformation. The interpretation of the CDF is straightforward because it has been defined[14] by the Laplacian of Vonk's multidimensional correlation function.[20] As such, it presents the autocorrelation of the surfaces from the colloidal domains in space similarly to Ruland's interface distribution function[21,22] for one-dimensional structures as a function of distance. For samples with fiber symmetry, the CDF [$z(r_{12}, r_3)$] is a function of two coordinates only (transverse direction, r_{12}, and fiber direction, r_3). Therefore, it can be displayed by means of contours or as a density plot in the plane. Positive peaks found in the vicinity of the origin are size distributions of the primary domains. Therefore, their size, shape, and orientation in space are depicted. Negative peaks following farther out exhibit long periods, that is, the distance of two adjacent domains from each other. Positive peaks following next describe the size and orientation of superdomains (i.e., assemblies made from two primitive domains separated by a rather probable distance and measured from the beginning of the first domain to the end of the second domain), and correlations among domains more distant are manifested in consecutive peaks at longer distances.

Finally, comments concerning the errors in the computation of the CDF will be made. In principle, the 2D detector only sees a sector of reciprocal space, which is, moreover, subject to statistical noise. However, because the outside range of the scattering pattern in reciprocal space is hardly structured, the information recorded is complete and describes the nanostructure in direct space almost exactly. Therefore, the kernel of the Fourier transformation (eq 1) is vanishing outside the recorded range, denoting that in real space the CDF can be reconstructed everywhere. Nevertheless, in practice, the discrete Fourier transformation is used anyway, but its resolution is increased by zero padding[23] (in this case to 0.5 nm).

Inevitably, there is noise in the scattering pattern recorded in reciprocal space, which, however, has little effect on the conclusions drawn concerning the nanostructure because it is low and in direct space has little effect on the topology information displayed in the CDF. The use of synchrotron radiation combined with long exposure provides for a tolerable signal-to-noise ratio that additionally is considerably reduced by the projection (eq 2). Assuming, for example, a remnant of perfect white noise, we can readily establish that its effect is a constant background to the CDF. Less simple models for noise may be treated in terms of a spatial frequency filter. In this case, the range of detectable order among the nanodomains becomes constrained.[14,16]

More difficult to assess is the effect on the presented nanostructure of iterating the background correction. In any case, iteration attenuates short-range correlations in the CDF considerably. As a result of increasing experience with comparing scattering patterns and CDFs, we are inclined to postulate that the CDF extracted without iteration shows, essentially, the distortions of nanostructure and hides, in a plentitude of random correlations, the regularity emerging from the scattering pattern.

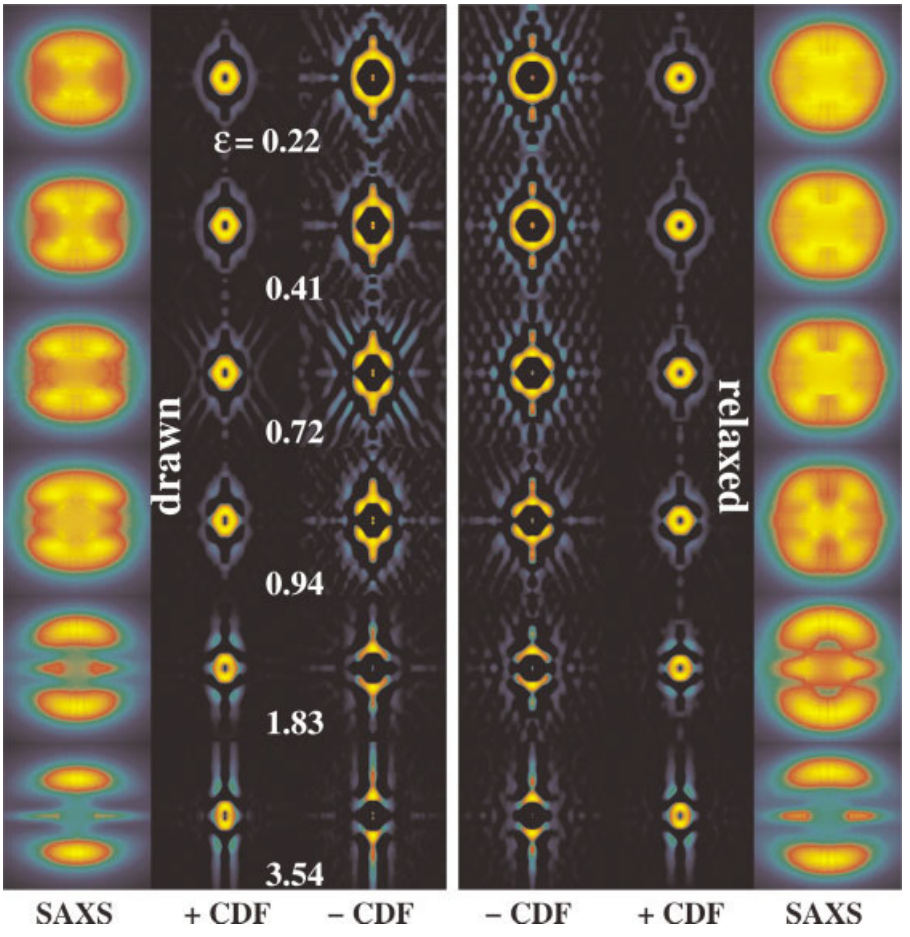

Figure 2. Arnitel E1500/50 as a function of ϵ. The SAXS patterns ($-0.15\ \mathrm{nm}^{-1} \leq s_{12}$, $s_3 \leq 0.15\ \mathrm{nm}^{-1}$) and CDFs exhibit the correlations of the hard and soft domains on a logarithmic scale in the interval $-45\ \mathrm{nm} \leq r_{12}, r_3 \leq 45\ \mathrm{nm}$. The straining direction is vertical. The left side shows patterns recorded in the drawn state, and the right side shows relaxation from the strain. +CDF indicates positive peaks, and −CDF indicates negative peaks.

RESULTS AND DISCUSSIONS

General Features of the Scattering and the CDF

A considerable disorder of the nanostructure in the initial material and its continuous improvement during the experiment are indicated from the results of the automated postprocessing of the scattering patterns. At $\epsilon = 0.22$, the elimination of the disordered background from the pattern requires seven steps, which decrease to five at $\epsilon = 0.72$ and finally to three for $\epsilon > 1.5$.

Figure 2 shows selected data from the drawn state on the left and corresponding data from the following measurements of the released sample on the right. The outer columns show the scattering patterns in pseudo-color. At low elongations, complex scattering patterns are observed. The corresponding butterfly patterns[24] are commonly interpreted by a nanostructure originating from stacks of tilted lamellae. The quantitative direct analysis of such a scattering pattern appears to be a challenging task with many uncertainties. As found earlier,[5,10,25] PEEs frequently exhibit a critical elongation, $\epsilon_{crit} \approx 1$, which is characterized by a considerable reduction of mechanical reversibility and a failure of the primary elastic network.

For Arnitel E1500/50, Figure 2 shows that, in principle, the scattering pattern does not change much up to $\epsilon = 1$, despite the considerable macroscopic elongation. A direct analysis of the patterns would probably resort to the determination

of peak positions and would relate these changes to variations both of long periods and orientations of the lamellae. Because of the only slight variations of the pattern, the significance of structure parameter changes determined directly from it would probably remain low, and the obvious reason is that any determination in reciprocal space is based on idealized notions.

In real space, the correlations among domain surfaces are visualized in the multidimensional CDF, which is shown in the four middle columns of Figure 2. Because the CDF shows both positive and negative peaks, each CDF is split into two parts labeled +CDF and −CDF, respectively.

The column labeled +CDF shows the positive peaks only. The most intense feature in all the patterns is the central ring, with the strongest maxima on the meridian. With increasing elongation, it grows ellipsoidally and indicates that the basic domain is granular or cylindrical. Therefore, we do not find homogeneous lamellae, as found in CDF studies on other polymers.[14,19] Only a small fraction of these domains are incorporated into the (correlated) nanostructure, which is responsible for the peaks in the SAXS pattern. This can be deduced from the fact that correlation peaks on the positive face of the CDF are weak. The domain height averaged over all the domains (correlated and uncorrelated ones) is 5–6 nm for all elongations, and the diameter is 5 nm or less. The question arises as to what feature makes the typical scattering pattern of stacks from tilted lamellae.

The column labeled −CDF shows the long periods of the nanostructure in real space. Here we observe that up to an elongation of $\epsilon = 0.72$, both the elongated and relaxed patterns show the same latticelike arrangement of cylindrical hard domains surrounding a central probe domain. This lattice is rigid and does not respond to alternating strain. As demonstrated later, each of the spots can be associated with the probability density of the top face of the corresponding hard domain. It is obvious that the stepped arrangement of hard domains approximates a lamella in two dimensions. At $\epsilon = 0.72$, the spots degenerate into lines that we suggest naming displacement lines. Before we explain why, let us first describe the general nanostructure of all the patterns below the critical elongation.

Nanostructure below the Critical Elongation

Figure 3 exemplifies the topological features of the nanostructure at low elongations, showing

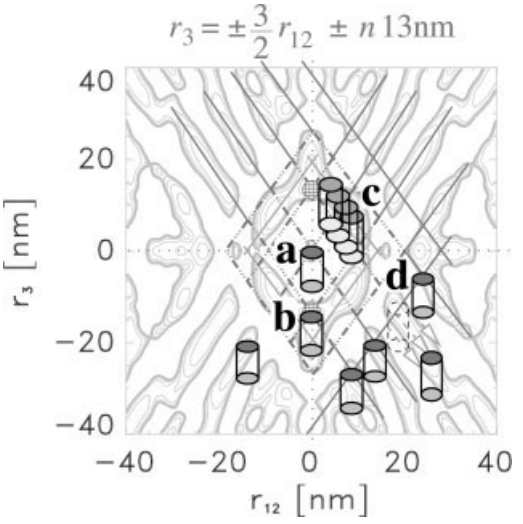

Figure 3. Arnitel E1500/50 at $\epsilon = 0.72$. A contour plot is shown for the CDF $[-z(r_{12}, r_3)]$ with lattice grid lines satisfying the equation $r_3(r_{12}) = \pm \frac{3}{2} r_{12} \pm n13\text{nm}$ with $n\varepsilon\{0, 1, \frac{3}{2}, 2, 3, \ldots\}$ and sketches of related hard domain cylinders.

the contours of the long period peaks in the CDF at $\epsilon = 0.72$. It is obvious that the spots and displacement lines form a set of grid lines that satisfy a set of linear equations:

$$r_3(r_{12}) = \pm\frac{3}{2} r_{12} \pm n\,13\text{nm} \qquad (3)$$

where n is (almost always) a natural number. In the outer part of the CDF correlation map, solid grid lines indicate that long period peaks are found on the grid. On the contrary, in the central region of $-z(\mathbf{r})$, minima are found on the grid, and this fact is indicated by dash–dot–dot–dot grid lines.

For the majority of the patterns, there are no displacement lines in the outer part, and so only spot-shaped long period peaks are found on the intersections of the grid lines. All the patterns show long period maxima even in the center of the CDF, but only two spots are normal with respect to the lattice that is manifested in the outer part. In the figure, these normal spots are indicated by cross-hatched circles. Additionally, there are strong long period maxima on the interstitial lines defined by $n = 3/2$ (solid, diamond-shaped contour). These reflections extend smoothly along the four grid lines.

Let us now interpret the pattern. For this reason, a hard domain probe is imagined to be placed in the center of the CDF. Without a restriction of the general validity, let us place it in such a way that the center of its top surface is put in the origin [Fig. 3(a)]. In this case, long period peak elevations are made from the correlations between only the top surfaces of two hard domain cylinders, but indentations are made from correlations between a top surface and a bottom surface, respectively. Because of this property, other hard domain cylinders now can easily be placed with the CDF map, as demonstrated in the figure.

Figure 3(b) indicates the placement of the next neighbor in the straining direction on the rigid lattice. The long period is 13 nm. Figure 2 shows that the position of the peak remains unchanged both in the strained and the relaxed state, but it becomes asymmetrically broadened in the strained state. Such broadening of X-ray lines was described many decades ago[26,27] and, with constant elasticity assumed, has been related to a variation of local stress in the material. In this case, a variation of local elasticity cannot be excluded, as was done in the early studies, but any combination of the of the two limiting physical reasons should result in the same mathematical description of the broadening by the Mellin convolution[28,29] of a basic long period distribution in the draw direction with a generating distribution associated with the distribution of stresses and elasticities.

Figure 3(c) indicates the placement of hard domains forming the interstitial long period. The elongated shape of the peak shows that the hard domains can be found anywhere along the line. This feature indicates either some kind of loose connectivity with the probe position or liquid-crystalline disorder of the hard domains forming the lamella. Both explanations suggest that there should be some response of this assembly of domains to external strain, as shown in Figure 2. In the strained state, the hard domains retract from the equator and partly recover during relaxation. Moreover, we observe that the interstitial position is marked not only by a ridge-shaped, off-meridional long period but also by a spot-shaped one residing on the meridian, which does not change its shape in the low elongation regime. In the meridional direction, this distance behaves rigidly.

Figure 3(d) shows the placement of hard domains in the colloidal lattice before a critical stress is reached. As long as the corresponding long period peaks exhibit the shape of a spot, the stepped arrangement of hard domains resembles an inclined layer and is related to the peculiar shape of the SAXS reflections, looking like intensity beams emerging from its center. From the mapped CDF, we can extract some more topological information concerning the shapes of these correlated cylindrical hard domains because the top surface has to reside on an elevation, whereas the bottom surface has to reside in a valley on the map. We find that the diameter of the correlated domains is about 5 nm and similar to the total average, but the height of the cylinders forming the lattice is bigger (8 nm) than the total average cylinder height.

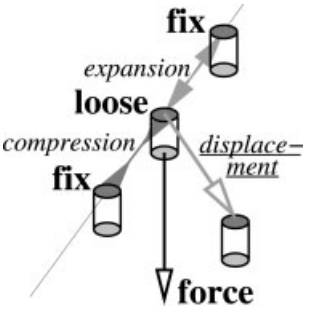

Figure 4. Explanation of the unique displacement process of loose hard domains from lamellae in PEE.

At an elongation of $\epsilon = 0.72$, the spots are degenerated into intensity ridges extending 20 nm along the direction of the grid lines. A possible formation process for these ridges is indicated below Figure 3(d). A single hard domain is torn from its original position in the lamella (dashed cylinder) and displaced (arrows) along an inclined direction. Therefore, we assume that at $\epsilon = 0.72$, we observe just the moment in which the formerly rigid lattice fails by pull-out, not of tie-molecules,[5,12] but of complete cylindrical hard domains.

Hard Domain Displacement Process

Now the question arises of why the cylinders pulled out are not straightly displaced in the direction of the drawing force, but instead in an inclined direction. We propose the explanation sketched in Figure 4.

Let us assume that the central domain is loose, whereas its closest neighbors are fixed in the layer. The drawing force is in the vertical direction. A movement of the cylinder in the vertical direction would cause a strong expansion of the

soft material connected to the upper cylinder, whereas the soft material connected to the lower neighbor would first slightly be compressed. To share the load between both connections, the loose cylinder draws aside and moves along the displacement line by a distance of up to 20 nm. No fine structure that would indicate preferential displacement distances is found.

Nanostructure above the Critical Elongation

After relaxation from $\epsilon = 0.72$ (cf. Fig. 2, right side, third row), the total recovery of the lattice structure is observed for the last time. After relaxing from $\epsilon = 0.94$, the lattice structure is deteriorated considerably, although the scattering pattern still shows four intensity beams emerging from the center. At elongations of $\epsilon > 1$, this destruction of the lamellar nanostructure becomes obvious even in the SAXS patterns. Both the SAXS two-point patterns and the CDF indicate the formation of a microfibrillar nanostructure with short-range order in the draw direction. Therefore, this nanostructure is generated from two but not many more hard domain cylinders arranged in a row oriented parallel to the draw; and this is the topological definition of a microfibril.

In Figure 2, we present few data from the microfibrillar state because it does not change considerably. Nevertheless, it seems noteworthy to mention that the meridional interstitial long period peak now responds to the cycling of strain, whereas the remains of the lattice long period (inner peak on the meridian) are almost unchanged.

In a previous work,[12] we studied a similar material, extracted the one-dimensional longitudinal structure, and addressed the microfibrillar component, which exhibited a short and constant long period by a slack component of microfibrils. No longer connected to the network, the microfibrils were said to no longer respond to strain. In this multidimensional CDF analysis, we observe that the short long period is more likely related to the fingerprint of a primary rigid lattice that has never responded to stress by an elastic process but has only failed and been broken into fragments.

CONCLUSIONS

The CDF itself is nothing but a real space representation of the scattering data. As such, it can be compared to the virtual image generated by shining light on a holographic screen. Therefore, it is better to ask for the significance of the algorithm than to ask for the limitations of the method. Here we have chosen an algorithm that iterates the SAXS background subtraction. As a result of this choice, the well-arranged, less distorted fraction of the nanostructure is emphasized in the CDF. This filtering is similar to what people are doing when they interpret SAXS patterns from their appearance. Therefore, this choice is best suited for identifying the nanostructural features that generate peculiar features in the SAXS patterns. It may be less suited to be compared to AFM images.

Similar to the information stored in a holographic screen, the CDF (virtual image) is interpreted more easily in terms of the nanoscale morphology than the scattering pattern (holographic screen) itself. Limitations arise from the emerging clarity itself because advancing toward a complete analysis now requires increased effort first to construct a complex mathematical model of the nanostructure and second to fit it to the scattering data.

The analysis of the CDF from a PEE has both shown remarkable symmetries concerning the nanostructure built from hard domains dispersed in a soft matrix and has revealed the peculiar displacement process by which the short-range colloidal lattice is converted into the ultimate microfibrillar structure. By carrying out similar studies on PEEs with a different composition, we expect to gain detailed information on the nanostructure evolution that may be valuable both for theoretical and practical considerations. At a high elongation, for example, the two different kinds of internal probes, each made from a pair of connected hard domains, may be useful in a study of local elastic properties in PEEs.

The SAXS measurements were supported by HASYLAB (Hamburg, Germany) through project II-01-41.

REFERENCES AND NOTES

1. Spontak, R. J.; Patel, N. P. Curr Opin Colloid Interface Sci 2000, 5, 334–341.
2. Statton, W. O. J Polym Sci 1962, 58, 205–220.
3. Statton, W. O. Z Kristallogr 1968, 127, 229–260.
4. Peterlin, A. Text Res J 1972, 42, 20–30.
5. Fakirov, S.; Fakirov, C.; Fischer, E. W.; Stamm, M. Polymer 1991, 32, 1173–1180.

6. Apostolov, A. A.; Fakirov, S. J Macromol Sci Phys 1992, 31, 329–355.
7. Fakirov, S.; Fakirov, C.; Fischer, E. W.; Stamm, M.; Apostolov, A. A. Colloid Polym Sci 1993, 271, 811–823.
8. Fakirov, S.; Denchev, Z.; Apostolov, A. A.; Stamm, M.; Fakirov, C. Colloid Polym Sci 1994, 272, 1363–1372.
9. Fakirov, S.; Fakirov, C.; Fischer, E. W.; Stamm, M. Polymer 1992, 33, 3818–3827.
10. Stribeck, N.; Sapoundjieva, D.; Denchev, Z.; Apostolov, A. A.; Zachmann, H. G.; Stamm, M.; Fakirov, S. Macromolecules 1997, 30, 1329–1339.
11. Bonart, R. Kolloid Z Z Polym 1966, 211, 14–33.
12. Stribeck, N.; Fakirov, S.; Sapoundjieva, D. Macromolecules 1999, 32, 3368–3378.
13. Stribeck, N. J Polym Sci Part B: Polym Phys 1999, 37, 975–981.
14. Stribeck, N. J Appl Crystallogr 2001, 34, 496–503.
15. Sauer, B. B.; McLean, R. S.; Brill, D. J.; Londono, D. J. J Polym Sci Part B: Polym Phys 2002, 40, 1727–1740.
16. Stribeck, N. Colloid Polym Sci 2002, 280, 254–259.
17. Buhmann, M. D. Acta Numer 2000, 9, 1–38.
18. Stribeck, N.; Buzdugan, E.; Ghioca, P.; Serban, S.; Gehrke, R. Macromol Chem Phys 2002, 203, 636–644.
19. Stribeck, N.; Bayer, R.; von Krosigk, G.; Gehrke, R. Polymer 2002, 43, 3779–3784.
20. Vonk, C. G. Colloid Polym Sci 1979, 257, 1021–1032.
21. Ruland, W. Colloid Polym Sci 1977, 255, 417–427.
22. Ruland, W. Colloid Polym Sci 1978, 256, 932–936.
23. Rosenfeld, A.; Kak, A. C. Digital Picture Processing; Academic: London, 1982; Vol. 1.
24. Murthy, N. S.; Grubb, D. T.; Zero, K. Proc Am Chem Soc PMSE Prepr 1998, 79, 363–364.
25. Stribeck, N.; Ghioca, P.; Buzdugan, E. J Appl Crystallogr 1997, 30, 708–711.
26. Dehlinger, U.; Kochendörfer, A. Z Kristallogr 1939, 101, 134–148.
27. Guinier, A. X-Ray Diffraction; Freeman: San Francisco, 1963.
28. Marichev, O. I. Handbook of Integral Transforms of Higher Transcendental Functions; Ellis Horwood: Chichester, England, 1983.
29. Stribeck, N. Colloid Polym Sci 1993, 271, 1007–1023.